# Automatic retinal vessel segmentation based on active contours method in Doppler spectral-domain optical coherence tomography

Wenzhong Liu
Tan Liu
Wei Song
Ji Yi
Hao F. Zhang

# Automatic retinal vessel segmentation based on active contours method in Doppler spectral-domain optical coherence tomography

Wenzhong Liu,[a] Tan Liu,[a] Wei Song,[a,b] Ji Yi,[a] and Hao F. Zhang[a,c]
[a]Northwestern University, Department of Biomedical Engineering, 2145 Sheridan Road, Evanston, Illinois 60208
[b]Harbin Institute of Technology, Department of Physics, 92 West Da-Zhi Street Nangang District, Harbin, Heilongjiang 150080, China
[c]Northwestern University, Feinberg School of Medicine, Department of Ophthalmology, 45 North Michigan Avenue, Suite 440, Chicago, Illinois 60611

**Abstract.** We achieved fast and automatic retinal vessel segmentation by employing the active contours method in Doppler spectral-domain optical coherence tomography (SD-OCT). In a typical OCT B-scan image, we first extracted the phase variations between adjacent A-lines and removed bulk motion. Then we set the initial contour as the boundary of the whole image and iterated until all of the segmented vessel contours became stabilized. Using a typical office computer, the whole segmentation took no more than 50 s, making real-time retinal vessel segmentation possible. We tested the active contours method segmentation in both controlled phantom and *in vivo* rodent eye images. © *2013 Society of Photo-Optical Instrumentation Engineers (SPIE).* [DOI: 10.1117/1.JBO.18.1.016002]

## 1 Introduction

Alterations in retinal blood flow velocity and volume can be associated with several ocular and systemic diseases, including, for example, ischemic optic neuropathy, glaucoma, diabetes, and HIV.[1–3] Accurately measuring blood flow can potentially help to better understand their pathophysiologies and to achieve early diagnosis of these diseases. Spectral-domain optical coherence tomography (SD-OCT) is a primary modality used to image the retinal anatomy with high spatial resolution.[4,5] By taking advantage of the Doppler effect impinging on the probing light induced by moving optical scatterers, OCT can measure retinal blood flow velocity, which further enables the OCT angiogram.[6–11]

Accurate estimation of blood flow volume in a retinal vessel requires OCT to obtain first, the spatial location and boundary of retinal vessels, second, the Doppler angles between the retinal blood flow and the OCT probing light, and third, the phase variance within the vessel caused by flowing blood. Spatial localization and boundary of a vessel could be obtained from OCT amplitude images,[12,13] which usually takes a long time, or by human operator,[6] which is subjective and lacks consistency among operators. Only after the spatial location and boundary of a vessel are identified, phase variance within the vessel boundary can be averaged for mean flow velocity, and centerline of the vessel can be further obtained to calculate the Doppler angle. From this point of view, retinal vessel segmentation is the key first step to achieve correct blood flow measuring.

Previously, histogram-based filtering[14] and support vector machine (SVM)[15] were used for retinal vessel segmentation in phase contrast OCT. Histogram-based filtering method worked well in images with high signal to noise ratios (SNRs); but showed poor results in relatively noisy images. Good segmentation results can also be acquired by SVM method; however, SVM method is time-consuming and requires a lengthy prior training. Here, we report a new, fast, and automatic vessel segmentation method for SD-OCT based on active contours method (ACM) and phase contrast.

## 2 Materials and Methods

### 2.1 Phantom and Animal Experiment

Both controlled phantom and *in vivo* rodent experiments were conducted. Phantom experiments were designed to test the accuracy of ACM segmentation. Specifically, a capillary tube was filled with a 1% Intralipid solution. The tube (CTPS125-250-5, Paradigm; inner diameter: 125 $\mu$m; outer diameter: 250 $\mu$m) was connected to a perfusion pump (A-99, Razel) at a flow rate of 9.92 $\mu$l/min. We imaged the phantom using a home-made SD-OCT system, which has been described in detail previously.[16] The OCT light source (IPSDD0804, InPhenix) has a center wavelength of 840 nm and a 3-dB bandwidth of 50 nm. The A-line rate was 24 kHz. The spatial resolutions of the SD-OCT in tissue were 6 $\mu$m (axial) and 20 $\mu$m (lateral). In total, 32 B-scans phantom images were acquired to test ACM segmentation accuracy, where results from all the 32 images were acquired independently and used to obtain mean and standard deviation (STD) of ACM segmentation result of the capillary tube. For comparison, histogram-based filtering segmentation was also performed.

Besides phantom experiment, we imaged rodent eyes *in vivo*. All animal experimental procedures were approved by the Institutional Animal Care and Use Committee at Northwestern

---

Address all correspondence to: Hao F. Zhang, Northwestern University, Department of Biomedical Engineering, 2145 Sheridan Road, Evanston, Illinois 60208. Tel: 847-491-2946; Fax: 847-491-4928; E-mail: hfzhang@northwestern.edu

University. Detailed information of the experimental procedure can be found in our previous paper.[17]

## 2.2 Preprocessing of Retinal SD-OCT Images

Figure 1 shows the preprocessing steps for *in vivo* SD-OCT images. Figure 1(a) is an SD-OCT fundus image of a rat eye, where the circle and arrow highlight the trajectory and direction of a circular scan around the optic disk. We first acquired a B-scan amplitude image containing 2048 A-lines [Fig. 1(b)] and further extracted the phase contrast [Fig. 1(c)] by subtracting the phase values between spatially adjacent A-lines. Then we corrected the bulk motion following the method reported in literature.[18] After that, we applied a $5 \times 15$
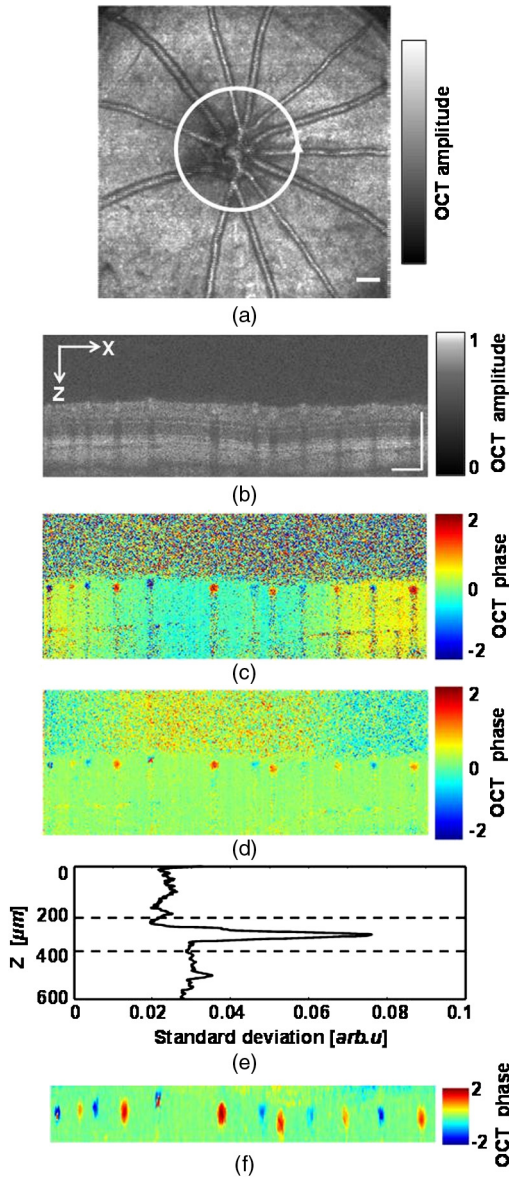


(a)

(b)

(c)

(d)

(e)

(f)

**Fig. 1** Preprocessing steps of *in vivo* rodent eye image. (a) OCT fundus image of rat retina. The circle highlights the scanning trajectory around the optic disk. Bar 200 $\mu$m; (b) OCT B-scan amplitude image from the position highlighted in panel a. Bar: 250 $\mu$m; (c) OCT B-scan phase image; (d) OCT B-scan phase image after bulk motion correction; (e) Phase STD distribution along the depth axis; and (f) reduced-size image OCT B-scan phase image.

median-filter for noise reduction to get a cleaner background in the phase contrast OCT image [Fig. 1(d)]. From both Fig. 1(c) and 1(d), we can observe that, indeed, all of the retinal blood vessels were located within a small depth range. In order to speed up the segmentation and improve the segmentation accuracy, we reduced the depth range of the OCT image and only applied ACM to the reduced region. The reduced-size image was determined by calculating the STD of the OCT phase variation along the horizontal axis. We observed that STD values were significantly higher within depth range exhibiting the highest vascular density compared to STD values from depth ranges without vessels [Fig. 1(e)]. Based on the calculated depth-resolved STD, we digitally removed the region beyond 100 pixels above and below the STD max [Fig. 1(f)].

## 2.3 Active Contours Method

The underlying principle of ACM is to evolve a contour enclosing the targeted objects in an image based on region-based gradient inside and outside the contour. A final contour may consist of boundaries of multiple objects.

According to Chan and Vese,[19] for a given image $I(x, y)$ in domain $\Omega$ (real number), ACM method is formulated by minimizing the energy $E$ defined by:

$$E = \int_{\text{inside}(C)} |I(x, y) - C_1|^2 \mathrm{d}x\mathrm{d}y$$
$$+ \int_{\text{outside}(C)} |I(x, y) - C_2|^2 \mathrm{d}x\mathrm{d}y, \qquad (1)$$

where $C$ is the contour, and $C_1$ and $C_2$ are the average intensities inside and outside the contour, respectively. Equation (1) can be solved iteratively through the following steps.

Step 1. Initialize a contour $C$ containing all the objects that are of interest. In the present study, the initial contour encompasses the boundary of the whole image. Then apply an initial level set (iteration index $k = 0$):

$$\varphi(x, y, k = 0) = \begin{cases} -1, & \text{outside}(C) \\ 1, & \text{inside}(C) \\ 0, & C \end{cases} . \qquad (2)$$

Step 2. Estimate $C_1$ and $C_2$ in Eq. (1):

$$C_1(\varphi) = \frac{\int_\Omega I(x, y) H(\varphi) \mathrm{d}x\mathrm{d}y}{\int_\Omega H(\varphi) \mathrm{d}x\mathrm{d}y} \qquad (3)$$

$$C_2(\varphi) = \frac{\int_\Omega I(x, y)[1 - H(\varphi)] \mathrm{d}x\mathrm{d}y}{\int_\Omega [1 - H(\varphi)] \mathrm{d}x\mathrm{d}y}, \qquad (4)$$

where

$$H(\varphi) = \begin{cases} 1, & \varphi \geq 0 \\ 0, & \text{otherwise} \end{cases} .$$

Step 3. Update the level set function with iteration number:[20]

$$\frac{\partial \varphi}{\partial k} = \frac{I(x, y) - \frac{C_1(\varphi) + C_2(\varphi)}{2}}{\max\left(\left| I(x, y) - \frac{C_1(\varphi) + C_2(\varphi)}{2} \right|\right)} \bullet \alpha |\nabla \varphi|, \qquad (5)$$

where $\alpha = 100$ is a factor to increase the segmentation speed, and $\nabla(\bullet)$ is the function estimating the gradient. The reason why we applied this level set function is that it improves the traditional level set methods by avoiding the estimation of the signed distance function (SDF) and re-initialization;[20] thus, it's more efficient.

Step 4.  Re-estimate $C_1$ and $C_2$ as in step 2 for the $(k + 1)$ iteration; then compare the results between the $k$th and $(k + 1)$th iterations. If the difference of $C_1$ and $C_2$ between the $k$th and $(k + 1)$th iterations are very small (such as $<10^{-5}$), the contour is stabilized, and segmentation is finished; otherwise, iteration continues. Although convergence may affect segmentation results very much, our tests of ACM segmentation typically converged within 100 iterations.

## 3  Results and Discussion

### 3.1  *Phantom Imaging Result*

We first tested the performance of ACM segmentation using a controlled phantom as shown in Fig. 2. Figure 2(a) is the OCT amplitude image of the capillary tube, where we can observe the Intralipid solution, the outer boundary, and the bottom of the container. The corresponding OCT phase image is shown in Fig. 2(b). After applying our algorithm described in Sec. 2.3, we extracted the boundary profile of the tube and further estimated the tube center based on the acquired boundary [Fig. 2(b)]. Based on the segmented result and the calibrated OCT resolutions, we estimated the inner diameter of the tube to be $126.67 \pm 2.92$ $\mu$m (after averaging 32 B-scan), which agreed with the specification ($125$ $\mu$m). The phantom imaging result confirmed the accuracy of the ACM segmentation method in OCT phase images. Figure 2(c) is the segmentation result using histogram-based filtering method and the estimated the tube's inner diameter was $129.31 \pm 3.15$ $\mu$m, which agreed with the specification. However, we can clearly observe segmentation errors in the background as pointed out by the arrows in Fig. 2(c).

### 3.2  *In Vivo Rodent Eye Imaging*

The segmentation results of the *in vivo* image are shown in Fig. 3. The boundaries and the center positions of all retinal vessels obtained from ACM are showed in Fig. 3(a). Altogether 12 vessels were identified by the algorithm, which agreed with our visual observation in the OCT fundus and amplitude OCT image [Fig. 1(a) and 1(b)]. By overlaying the detected boundaries onto the OCT phase image; we segmented all the retinal vessels from
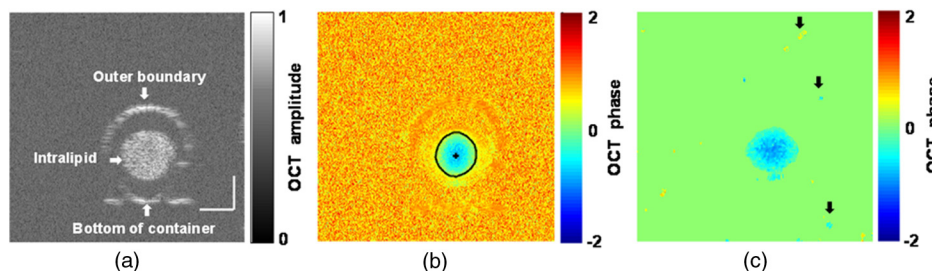


**Fig. 3** Segmentation results of *in vivo* retinal image. (a) Vessel boundaries and centers obtained from ACM method. Bar: 100 $\mu$m; (b) OCT phase image after all vessels are segmented; (c) segmentation results from histogram-based filtering method. The color bars in panels b and c represent OCT phase variation; and (d) comparison of estimated vessel diameters obtained by the two segmentation methods.

the background as shown in Fig. 3(b). The color in Fig. 3(b) represents the direction of the blood flow. Based on the size of the vessels and the magnitude of phase variances, it is reasonable to hypothesize that the venous blood flows outwards (red) and arterial blood flows inwards (blue) with respect to the image plane. Moreover, the vessels no. 1 and no. 5 (from the left) in Fig. 3(b) showed phase wrap, presumably caused by high flow velocity of the arterial blood; however, ACM is not affected by such phase wrap. We tested *in vivo* images from 10 rodent eyes (data not shown); the segmentation results were similar to Fig. 3.

Once the boundaries and center positions of all vessels are obtained, accurate calculation of mean vessel phase variation and the Doppler angle for complete retinal blood flow measurements can proceed. During the whole segmentation and center identification processes, we provided no user input. As a comparison, we showed the segmentation result using the histogram-based filtering method[14] in Fig. 3(c). Although all vessels were segmented, the boundaries are not as uniform as Fig. 3(b), and it also has a noisy background (as pointed out by arrows), all of which may affect further information extraction based on the



**Fig. 2** Imaging and segmentation results of the capillary tube phantom. (a) OCT B-scan amplitude image. Bar: 100 $\mu$m; (b) ACM segmentation results overlaid on OCT B-scan phase image. The black circle is detected contour and black cross is the calculated vessel center; and (c) Histogram-based filtering segmentation result.
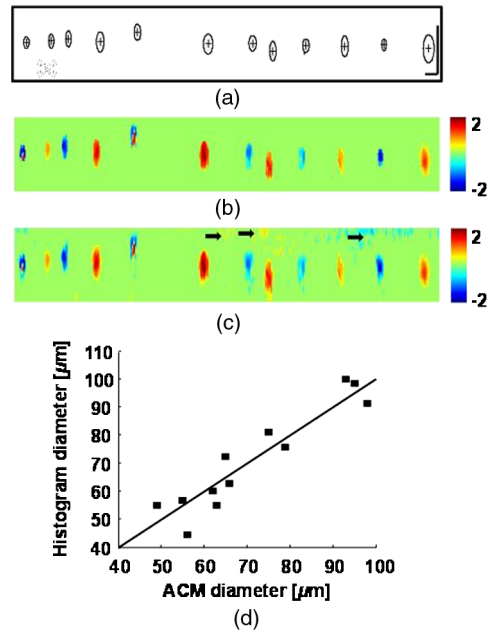
segmented results. Vessel diameters obtained from both ACM and histogram-based filtering were compared [Fig. 3(d)] and they, in general, agreed with each other. However, we cannot conclude which method is more precise because there is no gold standard to measure retinal vessel diameters *in vivo*.

We also tested the speed of our ACM segmentation in ten different *in vivo* OCT B-scan images with the same image size (2048 points per A-line, 4096 A-lines per B-scan). Using a typical office laptop (Thinkpad™ T400 with RAM 2 GB and Intel™ P8600 Processor at 2.4 GHz), our Matlab™ (Math-Works, version 2011a) code took $12.17 \pm 0.046$ s for OCT raw image reconstruction, $1.28 \pm 0.0052$ s for Doppler signal extraction, and $11.09 \pm 2.12$ s for ACM segmentation. The histogram-based filtering was faster than ACM in image segmentation, where $0.25 \pm 0.02$ s was needed in the segmentation step. However, the results from histogram-based method were not as good as results from ACM. Such performance of ACM can allow real-time clinical applications in the future if we further optimize the algorithm and, especially, take advantage of advanced hardware such as graphic processing unit.[21,22]

## 4 Conclusion

In this work, we applied a fast and automatic retinal vessel segmentation method, active contours method, in phase contrast OCT images. We first examined the segmentation accuracy of the ACM in controlled phantom experiments. In an Intralipid-filled capillary tube, the measured inner diameter agreed well with the manufacturer specification. Then we tested our method in multiple *in vivo* rodent retinal images. In every tested image, we obtained all the vessel boundaries and vessel centers with a processing time less than 1 min. The significance of ACM method lies in its automatic capabilities in obtaining vessel centers and boundaries fast, which permits future real-time operations and better estimation of Doppler angles and blood flow velocities in clinical settings.

### References

1. L. Padnick-Silver et al., "Retinal oxygenation and oxygen metabolism in Abyssinian cats with a hereditary retinal degeneration," *IOVS* **47**(8), 3683–3689 (2006).
2. D. G. Puro, "Retinovascular physiology and pathophysiology: new experimental approach/new insights," *Prog. Retin. Eye Res.* **31**(3), 258–70 (2012).
3. K. Polak et al., "Regulation of human retinal blood flow by endothelin-1," *Exp. Eye Res.* **76**(5), 633–640 (2003).
4. M. Wojtkowski et al., "*In vivo* human retinal imaging by Fourier domain optical coherence tomography," *J. Biomed. Opt.* **7**(3), 457–463 (2002).
5. V. J. Srinivasan et al., "Ultrahigh-speed optical coherence tomography for three-dimensional and en face imaging of the retina and optic nerve head," *IOVS* **49**(11), 5103–5110 (2008).
6. Y. Wang et al., "Retinal blood flow measurement by circumpapillary Fourier domain Doppler optical coherence tomography," *J. Biomed. Opt.* **13**(6), 064003 (2008).
7. R. K. Wang and L. An, "Doppler optical micro-angiography for volumetric imaging of vascular perfusion *in vivo*," *Opt. Express* **17**(11), 8926–8940 (2009).
8. Z. Zhi et al., "Impact of intraocular pressure on changes of blood flow in the retina, choroid, and optic nerve head in rats investigated by optical microangiography," *Biomed. Opt. Express* **3**(9), 2220–2233 (2012).
9. J. Zhang and Z. Chen, "*In vivo* blood flow imaging by a swept laser source based Fourier domain optical Doppler tomography," *Opt. Express* **13**(19), 7449–7457 (2005).
10. B. White et al., "*In vivo* dynamic human retinal blood flow imaging using ultra-high-speed spectral domain optical coherence tomography," *Opt. Express* **11**(25), 3490–3497 (2003).
11. J. Walther et al., "Optical coherence tomography in biomedical research," *Anal. Bioanal. Chem.* **400**(9), 2721–2743 (2011).
12. M. Pilch et al., "Automated segmentation of retinal blood vessels in spectral domain optical coherence tomography scans," *Biomed. Opt. Express* **3**(7), 1478–1491 (2012).
13. H. Wehbe et al., "Automatic retinal blood flow calculation using spectral domain optical coherence tomography," *Opt. Express* **15**(23), 15193–15206 (2007).
14. C. Kolbitsch, T. Schmoll, and R. A. Leitgeb, "Histogram-based filtering for quantitative 3D retinal angiography," *J. Biophoton.* **2**(6–7), 416–425 (2009).
15. A. S. G. Singh, T. Schmoll, and R. A. Leitgeb, "Segmentation of Doppler optical coherence tomography signatures using a support-vector machine," *Biomed. Opt. Express* **2**(5), 1328–1339 (2011).
16. T. Liu et al., "Combined photoacoustic microscopy and optical coherence tomography can measure metabolic rate of oxygen," *Biomed. Opt. Express* **2**(5), 1359–1365 (2011).
17. W. Song et al., "Integrating photoacoustic ophthalmoscopy with scanning laser ophthalmoscopy, optical coherence tomography, and fluorescein angiography for a multimodal retinal imaging platform," *J. Biomed. Opt.* **17**(6), 061206 (2012).
18. V. Yang et al., "High speed, wide velocity dynamic range Doppler optical coherence tomography (part I): system design, signal processing, and performance," *Opt. Express* **11**(7), 794–809 (2003).
19. T. F. Chan and L. A. Vese, "Active contours without edges," *IEEE Trans. Image Process.* **10**(2), 266–277 (2001).
20. K. Zhang et al., "Active contours with selective local or global segmentation: a new formulation and level set method," *Image Vis. Comput.* **28**(4), 668–676 (2010).
21. K. Zhang and J. U. Kang, "Real-time 4D signal processing and visualization using graphics processing unit on a regular nonlinear-k Fourier-domain OCT system," *Opt. Express* **18**(11), 11772–11784 (2010).
22. Y. Huang, X. Liu, and J. U. Kang, "Real-time 3D and 4D Fourier domain Doppler optical coherence tomography based on dual graphics processing units," *Biomed. Opt. Express* **3**(9), 2162–2174 (2012).